J. Electrochem. Sci. Eng. **16** (2026) 2998; http://dx.doi.org/10.5599/jese.2998

Open Access : ISSN 1847-9286
https://pub.iapchem.org/ojs/index.php/JESE

Original scientific paper

Tunable electrochemical properties of polyaniline/CuO/$BaTiO_3$ nanocomposites for supercapacitor application

Geethu Joseph[1], Aryadevi Gopinath[2], Veena Rose Mathew[1], Alex Jose[1], Alex Joseph[3], Santhosh Kumar Raghavan Pillai[4], Esha Devaraj Suja[1] and Ginson P. Joseph[1,✉]

[1]*Material Science Research Lab, Department of Physics, St. Thomas College Palai, Kerala 686574, India*
[2]*Department of Physics, CMS College (Autonomous), Kottayam, Kerala, 686001, India*
[3]*Department of Chemistry, Newman College, Thodupuzha, Idukki, Kerala, 685585, India*
[4]*Department of Physics, St. George's College, Aruvithura, Kottayam, Kerala, 686122, India*
Corresponding authors: ✉*ginsonpj@gmail.com*; Tel. 9447064652

Received: September 5, 2025; Accepted: October 29, 2025; Published: November 4, 2025

Abstract

Revolutionizing energy storage demands innovative strategies that transcend the conventional boundaries of electrode design. Here, we unveil a powerful approach that harnesses the synergistic interplay between dielectric and conductive nanophases to unlock unprecedented charge storage performance in polymeric supercapacitors. By individually synthesizing copper oxide (CuO) and barium titanate ($BaTiO_3$) nanoparticles and strategically embedding them into a polyaniline (PANI) matrix, we engineered two finely tuned ternary nanocomposites: PCB5 (10 wt.% CuO, 5 wt.% $BaTiO_3$) and PCB10 (5 wt.% CuO, 10 wt.% $BaTiO_3$). Advanced structural and spectroscopic analyses (X-ray diffraction, field emission scanning electron microscopy, energy-dispersive X-ray spectroscopy, X-ray photoelectron spectroscopy, Raman spectroscopy) confirmed the successful integration of the nanophases, while dielectric studies revealed distinct variations in dielectric constant and interfacial polarization behaviour depending on nanoparticle ratios. Among the composites, PCB5 showed the most balanced electrochemical performance, with a specific capacitance of 271.67 F g^{-1}, outperforming pristine PANI and its $BaTiO_3$-rich counterpart. Electrochemical impedance spectroscopy further confirmed the low series and charge-transfer resistances of the PCB5 composite sample, reflecting its efficient ion/electron transport pathways. Furthermore, BET analysis showed an increased surface area (31.37 m^2 g^{-1}) compared to pristine PANI (24.08 m^2 g^{-1}), providing additional electroactive interfaces for charge accumulation. These findings establish, for the first time, a dielectric-conductive co-engineering paradigm in PANI nanocomposites, where carefully optimized filler ratios act as a dual-function booster of both dielectric constant and electrochemical kinetics. This extraordinary synergy paves the way for transformative next-generation high-energy, high-power supercapacitors with tunable multifunctionality.

Keywords
Dielectric, ferroelectric ceramics; polyaniline matrix; energy storage; specific capacitance

Introduction

Supercapacitors have emerged as a pivotal energy storage technology, distinguished by their ultrahigh power density, rapid charge-discharge capability, and long cycle stability-attributes that align seamlessly with the escalating global demand for efficient, reliable, and sustainable energy storage solutions [1,2]. Conducting polymers such as polyaniline (PANI) have garnered significant interest among different electrode materials because of their superior pseudocapacitive behaviour, simplicity in production, environmental stability, and adjustable redox characteristics [3]. To improve PANI's electrochemical performance, functional nanomaterials must be added due to its inherent drawbacks, which include restricted surface area and moderate cycle stability.

Enhancing conductivity, surface area, and electrochemical stability through the incorporation of metal oxide nanoparticles into PANI matrices has been the subject of much research [3]. Because of its high theoretical specific capacitance, natural availability, affordability, and environmental friendliness, copper oxide (CuO), a p-type transition metal oxide, has been the subject of extensive research [4]. The structural instability and low electrical conductivity of CuO during long-term cycling, however, can be mitigated by embedding it in a conductive polymer matrix such as PANI.

In contrast, barium titanate ($BaTiO_3$), a perovskite-type dielectric material, is a desirable option for improving charge storage capacity and dielectric responsiveness in composite electrodes due to its strong ferroelectric characteristics and high dielectric constant [5,6]. The hybrid electrode structure's interfacial polarization and ionic/electronic channels can both be modulated with the use of $BaTiO_3$ nanoparticles [6].

The judicious combination of both conductive and dielectric nanoparticles within a conducting polymer matrix offers a unique approach to simultaneously optimize charge transport pathways and enhance charge storage mechanisms, addressing the multifaceted requirements for high-performance supercapacitor electrodes. Recent studies on PANI-based nanocomposites have shown that incorporating 5 to 10 wt.% of inorganic nanoparticles often leads to marked improvements in conductivity, dielectric behaviour, and electrochemical performance without causing significant particle agglomeration or conductivity suppression. For instance, in situ synthesis of PANI/CuO nanocomposites with 5-15 wt.% CuO revealed enhanced charge transfer and pseudocapacitance, with optimal performance observed around the 10 wt.% range [7]. Similarly, $BaTiO_3$-PANI composites containing 5 wt.% $BaTiO_3$ displayed a strong increase in dielectric constant, supporting the idea that lower nanoparticle loadings are effective for tailoring dielectric properties without disrupting polymer morphology [6]. Moreover, mixed-metal oxide/PANI systems (*e.g.* TiO_2-CuO/PANI) have successfully employed comparable concentration regimes to achieve synergistic functionality by exploiting both conductivity and dielectric attributes [8].

Building on this foundation, we report on a novel co-engineering strategy that exploits the synergistic interaction of conductive copper oxide (CuO) and dielectric barium titanate ($BaTiO_3$) nanoparticles within a polyaniline (PANI) matrix to create advanced supercapacitor electrodes. Unlike prior studies that examine these fillers in isolation, our work systematically varies their ratios to disentangle and harness their complementary roles. Two tailored formulations were developed: PCB5 (10 wt.% CuO, 5 wt.% $BaTiO_3$), designed to maximize charge transport, and PCB10 (5 wt.% CuO, 10 wt.% $BaTiO_3$), engineered to enhance dielectric polarization. This rational doping approach enables precise tuning of conductivity and interfacial polarization, directly overcoming the limitations of pristine PANI electrodes. Comprehensive structural, dielectric, and electrochemical characterizations confirm the

emergence of a delicate balance between electron mobility and dielectric response, culminating in electrodes with markedly improved capacitance and energy density. By demonstrating a multi-functional filler synergy within a conducting polymer host, this study establishes a forward-looking design principle for next-generation high-performance supercapacitors.

The central innovation of this work lies in the deliberate co-engineering of conductive (CuO) and dielectric ($BaTiO_3$) nanofillers within a polyaniline (PANI) matrix to realize a new class of super-capacitor electrodes. While the individual roles of conductive and dielectric phases have been extensively documented, their combined, systematically tuned integration within a single conducting polymer framework remains largely unexplored. By strategically balancing these complementary nanophases, we demonstrate how interfacial polarization and charge transport can be simultaneously optimized, an achievement rarely reported in polymer-based energy storage research. This study establishes a new paradigm in which inorganic fillers do not merely enhance individual properties but also act cooperatively with the conducting polymer host to yield electrodes with superior electrochemical kinetics and dielectric response. The insights gained here extend beyond incremental improvements, pointing toward a rational design strategy for next-generation high-performance, multifunctional supercapacitors.

Experimental

Materials

All chemicals used in this study were of analytical grade and procured from Merck, India. Barium hydroxide octahydrate ($Ba(OH)_2{\cdot}8H_2O$) (≥98 %, CAS No. 12230-71-6), titanium dioxide (TiO_2) (≥99 %, CAS No. 13463-67-7), copper(II) sulphate pentahydrate ($CuSO_4{\cdot}5H_2O$) (≥98 %, CAS No. 7758-99-8), sodium hydroxide (NaOH, ≥98 %, CAS No. 1310-73-2), aniline (≥98 %, CAS No. 62-53-3), ammonium persulfate (APS, ≥98 %, CAS No. 7727-54-0) and hydrochloric acid (HCl, 35 to 38 %, CAS No. 7647--01-0) were used as received without further purification. Deionized water was used throughout all synthesis and processing steps.

Synthesis of copper oxide nanoparticles

Copper oxide nanoparticles were synthesized *via* a simple precipitation method using $CuSO_4{\cdot}5H_2O$ and NaOH as precursors. Initially, an aqueous solution of 0.1 M $CuSO_4{\cdot}5H_2O$ was prepared and stirred continuously to ensure complete dissolution. Separately, 0.2 M NaOH solution was prepared and added dropwise to the copper sulphate solution under vigorous magnetic stirring at room temperature. Upon addition, a pale blue precipitate formed, which gradually turned black, indicating the formation of CuO nanoparticles. The reaction mixture was stirred for an additional 2 hours to ensure complete precipitation and aging of the product. The black precipitate was then filtered, thoroughly washed several times with deionized water and ethanol to remove residual ions and by-products, and subsequently dried in a hot air oven at 70 °C for a few hours. For improved crystallinity, the dried powder was optionally calcined at 500 °C for 2 hours in a muffle furnace.

Synthesis of barium titanate nanoparticles

Barium titanate nanoparticles were synthesized *via* the hydrothermal method using barium hydroxide octahydrate and titanium dioxide as precursors (Equation 1).

$$Ba(OH)_2 + TiO_2 \rightarrow BaTiO_3 + H_2O \quad (1)$$

The molar ratio of Ba to Ti was maintained at 1:1. Barium hydroxide (1.35 g) was dissolved in 60 mL of deionized water under continuous stirring until a clear solution was obtained. 0.343 g TiO_2

is added to the above solution and stirred again for an hour. The components were homogenized by continuous stirring at room temperature, then transferred to a Teflon-coated autoclave and heated to 150 °C in a muffle furnace for 4 hrs. It is taken and washed a few times and dried. Then, it was calcined at 600 °C for 3 hours to obtain white $BaTiO_3$ nano-powder.

Synthesis of polyaniline/CuO/$BaTiO_3$ nanocomposite

The ternary composite was synthesized *via* oxidative polymerization of aniline using ammonium persulfate (APS) as the oxidant in an acidic medium. 5 wt.% of barium titanate nanoparticles, along with 10 wt.% copper oxide nanoparticles were first ground in a mortar. Then, the mixture was dispersed in 100 mL of 1 M HCl solution and stirred for 30 minutes and then sonicated to achieve uniform dispersion. Aniline (1.86 g, 0.02 mol) was then added to the above dispersion under constant stirring to maintain a 0.2 M concentration. Separately, APS (4.56 g, 0.02 mol) was dissolved in 100 mL of deionized water to prepare a 0.2 M oxidant solution. The APS solution was added dropwise to the aniline solution over 30 minutes under continuous stirring in an ice bath maintained at 0-5 °C to control the polymerization rate. After the oxidant was fully added, the reaction mixture was stirred for an additional 5 hours to ensure complete polymerization. The resulting dark green precipitate was allowed to settle overnight at room temperature. The precipitate was collected by filtration and washed thoroughly with deionized water until the filtrate reached neutral pH. Finally, dried at 120 °C for 5 hours in a muffle furnace to obtain fine-powdered PANI-CuO- $BaTiO_3$ nanopowder samples, represented as PCB5.

The other composite, denoted PCB10, is synthesized using the same method as above, interchanging the dopant weight percentages.

Instrumentation

X-ray diffraction (XRD) (Rigaku Miniflex 6000 Cu Kα 0.15406 nm) at a voltage of 40 kV and a current of 15 mA was employed for the initial structural characterization of the samples. A scanning rate of 0.02 *per* s was used to record the patterns in the 2θ range of 10 to 80°. The MAIA3XMH field emission scanning electron microscope (FE-SEM) with energy-dispersive technology (TESCAN, Czech Republic) was used in this investigation. A thin layer of each nanoparticle sample (PANI, PCB5 and PCB10) was deposited on carbon tape affixed to aluminium stubs, vacuum-dried at 60 °C for 12 h, and sputter-coated with gold (20 mA, 60 s).

FE-SEM imaging and energy-dispersive X-ray spectroscopy (EDX) mapping were performed under high vacuum at 20 kV with an acquisition time of 60 s per area to assess elemental composition. X-ray photoelectron spectroscopy (XPS) was performed using a Thermo Scientific ESCALAB Xi+ system (Thermo Fisher Scientific, USA) to analyse the elemental composition and chemical states of the samples. For Raman spectroscopy, we employed an Alpha 300RA Confocal Raman Microscope integrated with an atomic force microscope (AFM) (WITec GmbH, Germany). The system used a 532 nm Nd: YAG laser as the excitation source, and the scattered light was captured with a Peltier-cooled CCD detector (576×384 pixels). A spectrograph with a holographic grating of 1800 lines *per* mm was used for spectral analysis.

Dielectric properties of the nanocomposite samples were measured using a HIOKI 3532-50 LCR HiTESTER (HIOKI E.E. Corporation, Japan). The powders were pressed into pellets of ~10 mm diameter and ~1 mm thickness using a hydraulic press. Silver paste was applied on both faces of each pellet to form electrodes and ensure good electrical contact. Capacitance, dielectric constant (ε'), and dielectric loss (ε'') were recorded over a frequency range of 100 Hz to 1 MHz at room temperature, allowing evaluation of AC conductivity and dielectric behaviour as a function of frequency.

The BET (Brunauer-Emmett-Teller) surface area analysis was conducted using a Surface Area Analyser (SMART/SA/01/16-17), manufactured by Smart Instruments (India), with the model SmartSorb 93. The analysis was performed using the BET single-point dynamic flow method, with nitrogen as the adsorbate gas. Using a dynamic flow technique, the device calculates the surface area based on gas adsorption at a given relative pressure (P/P_0). To remove surface impurities, the samples were degassed under carefully controlled conditions before analysis. Accurate surface area measurement is ensured by the system's precise gas flow rate and detection mechanism.

Electrochemical studies were performed using a Metrohm Autolab potentiostat/galvanostat (Model No. PGSTAT302N, Metrohm, Netherlands) equipped with Nova 2.1 software. Electrochemical studies involve cyclic voltammetry (CV), galvanostatic charge discharge (GCD) and electrochemical impedance spectroscopy (EIS). Also, the variation of electrochemical properties with respect to the structural nature of the composites is also compared and analysed. The electrochemical behaviour of the synthesized samples was evaluated using a standard three-electrode configuration. For the working electrode preparation, 5 mg of the active material was dispersed in 1 mL of deionized water by ultrasonication, followed by vigorous stirring to obtain a uniform slurry. A 60 µL portion (≈ 0.30 mg) of this dispersion was drop-cast onto a pre-polished glassy carbon electrode (GCE) using a micro-pipette and dried at room temperature to form the working electrode film. The platinum wire and Ag/AgCl (3 M KCl) electrodes were used as the counter and reference electrodes, respectively. All electrochemical measurements were carried out in 1 M H_2SO_4 aqueous electrolyte within the potential range of -0.2 to +1.0 V (*vs*. Ag/AgCl). Cyclic voltammetry, galvanostatic charge-discharge and electrochemical impedance spectroscopy measurements were recorded under identical conditions for all samples to ensure comparability. The Nyquist plots were recorded using a sinusoidal perturbation of 5 mV over a frequency range of 100 kHz to 0.01 Hz at the open-circuit potential (~0 V *vs*. Ag/AgCl) to evaluate charge transfer and ion-diffusion behaviour at the electrodes.

Results and discussion

Structural analysis

The XRD patterns of the synthesized $BaTiO_3$ and CuO nanoparticles are shown in Figure 1(a). The XRD of CuO confirms a monoclinic crystal structure [4]. Prominent diffraction peaks obtained at 2θ = 32.58, 35.47, 38.97 and 48.74° correspond to (110), (002), (200) and (202) as in JCPDS card No: 48-1548 [9]. The XRD pattern fits well with the peak positions of the standard cubic phase $BaTiO_3$ (JCPDS No. 31-174). It is also observed that a relatively strong additional diffraction peak appears at approximately $2\theta \approx 28°$, which corresponds to barium carbonate ($BaCO_3$) in the witherite phase (JCPDS No. 45-1471). A very weak reflection near $2\theta \approx 28°$ can also be assigned to the (200) plane of $BaCO_3$ (JCPDS No. 45-1471, 2θ = 27.7°). The formation of $BaCO_3$ impurities is attributed to the reaction of residual Ba^{2+} ions with atmospheric CO_2 during the drying process [5]. The additional weak peaks beyond the standard cubic $BaTiO_3$ pattern (JCPDS 31-0174) are attributed to minor structural distortions and trace secondary phases commonly observed in nanocrystalline $BaTiO_3$. Local tetragonal microdomains or oxygen-vacancy-induced superstructures may produce weak extra reflections, and traces of unreacted TiO_2 can also contribute to these peaks. The low values indicate high crystallinity. Tetragonal phase means peak splitting around 45°, but for a 1:1 precursor ratio (Ba:Ti) no splitting is observed [10].

The Scherrer equation is a commonly used formula for estimating the average crystallite size of a substance from the width of its XRD peaks. It can be represented by Equation (2) [11]:

$$D = \frac{k\lambda}{\beta \cos\theta} \quad (2)$$

where *D* is the average crystallite size, *k* is the shape factor (typically taken as 0.9), λ is the wavelength of the X-rays used (for Cu Kα radiation, λ = 0.15406 nm), β is the full width at half maximum (FWHM) of the peak in radians, and θ is the diffraction angle in degrees.

The size of the crystallites, denoted as *D*, is inversely correlated with the broadening of the peaks observed in the XRD pattern (indicated by β). A narrower peak signifies a larger crystallite size, whereas a broader peak signifies a smaller crystallite size. In this investigation, the crystallite sizes of the $BaTiO_3$ and CuO nanoparticles were determined using the Scherrer equation to be 100 and 80 nm, respectively. This measurement indicates the presence of nanoscale crystallites within the material, thereby confirming its nanocrystalline characteristics.

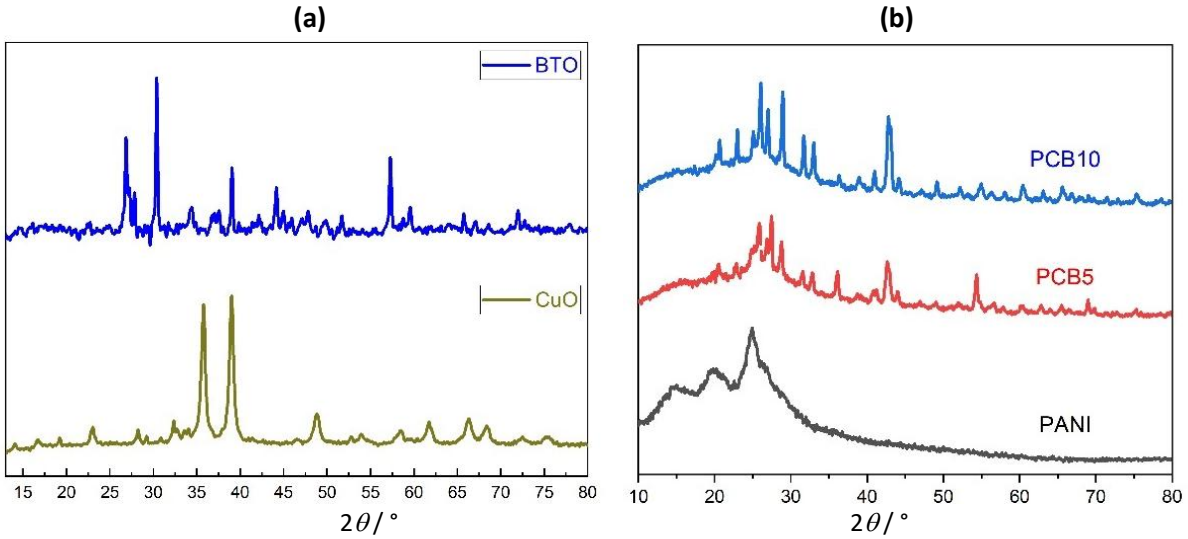

Figure 1. *XRD spectra of (a) $BaTiO_3$ and CuO nanoparticles, (b) pristine polyaniline (PANI) and PANI/$BaTiO_3$/CuO composites PCB5 and PCB10*

Field-emission scanning electron microscopy was used to visualize the size and surface morphology of the nanoparticles in high resolution. This method gave precise details on the particles' size, shape, and state of aggregation.

Figure 2(a) shows the FESEM image of PANI, while Figure 2(b) shows the FESEM image of PCB5, where small dots correspond to the doped nanoparticles. FESEM image of PCB10 is presented in Figure 3(c). Representative EDX spectra of PCB5 and PCB10 composite samples are shown in Figure 2(d) and 2(e), confirming the presence of all intended constituent elements. For PCB5, the Cu weight percentage was notably higher than that of Ba, reflecting its higher CuO loading (10 wt.%) compared to $BaTiO_3$ (5 wt.%). Conversely, PCB10 displayed elevated Ba content, consistent with its higher BaTiO3 concentration (10 wt.%) compared with CuO (5 wt.%). These quantitative elemental distributions obtained from EDX analysis validate the intended compositional formulations of the synthesized composites and align well with their designed weight ratios. Similar EDX confirmation of metal oxide incorporation in polymer matrices has been reported in the literature [12], reinforcing the reliability of the current observations.

Figure 3(a) presents the high-resolution XPS spectra of the composite samples, clearly exhibiting the characteristic peaks corresponding to Ba 3d, Ti 2p, and Cu $2p_3$, thereby confirming the successful incorporation of $BaTiO_3$ and CuO into the polyaniline (PANI) matrix. A notable increase in the intensity of the Ba 3d signal is observed in the composite, indicating a higher concentration or enhanced surface exposure of Ba species.

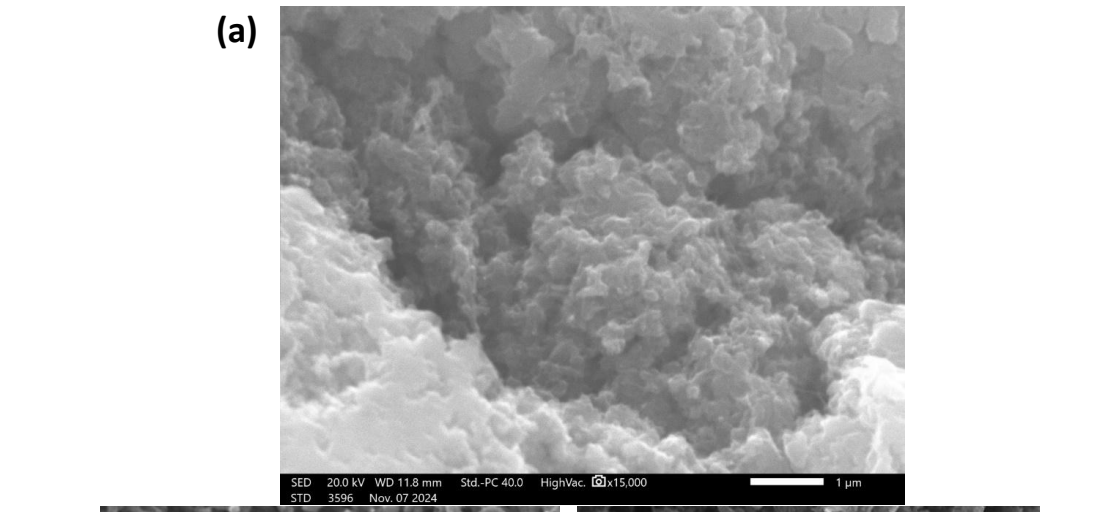

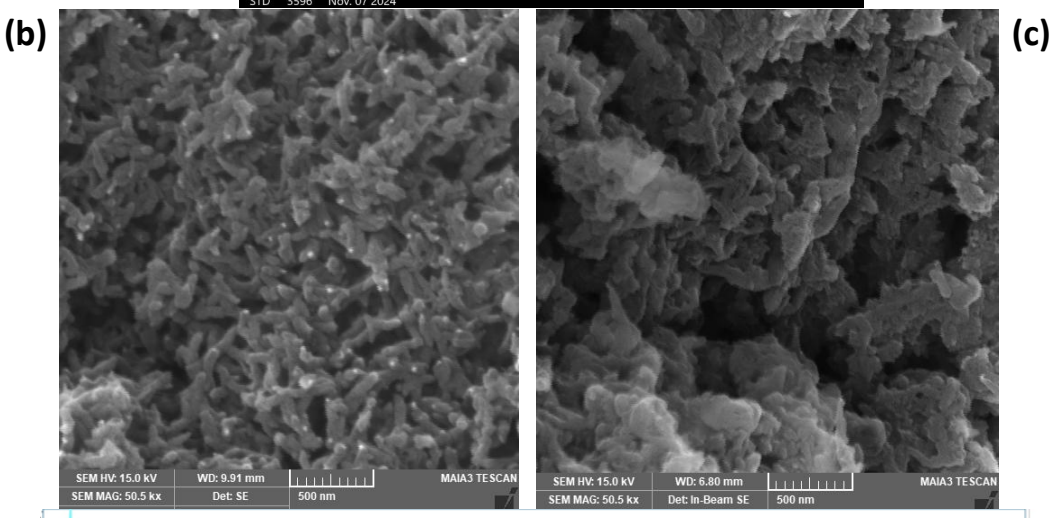

(d)

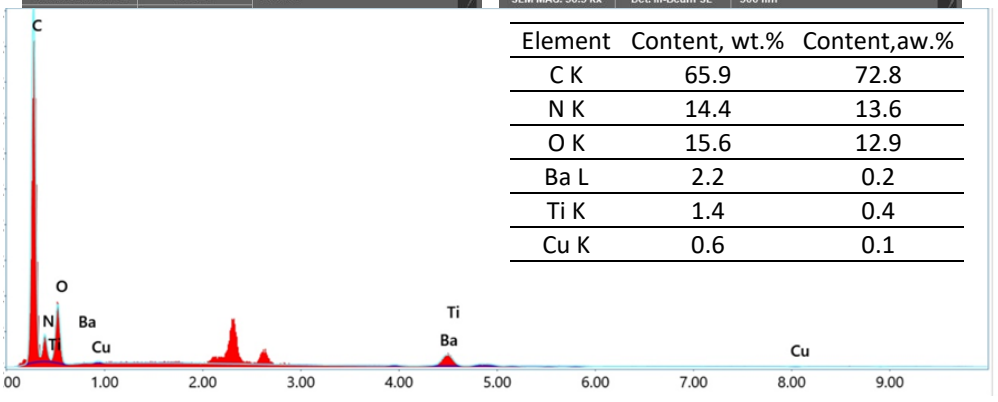

Element	Content, wt.%	Content,aw.%
C K	65.9	72.8
N K	14.4	13.6
O K	15.6	12.9
Ba L	2.2	0.2
Ti K	1.4	0.4
Cu K	0.6	0.1

(e)

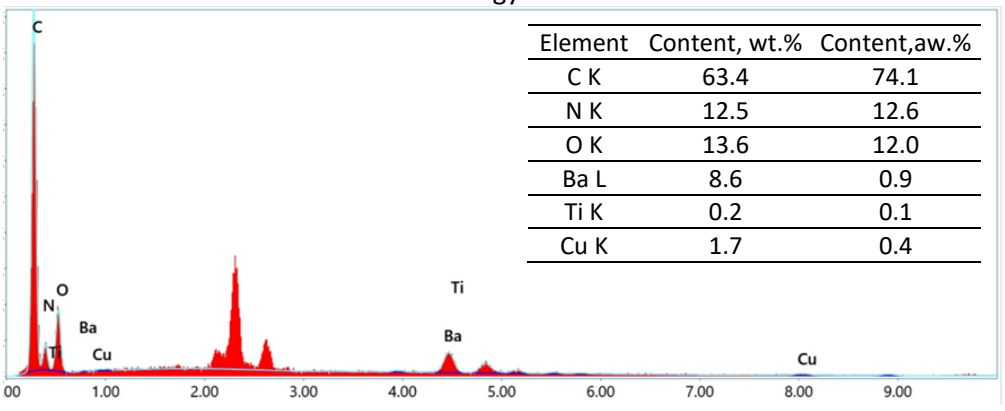

Element	Content, wt.%	Content,aw.%
C K	63.4	74.1
N K	12.5	12.6
O K	13.6	12.0
Ba L	8.6	0.9
Ti K	0.2	0.1
Cu K	1.7	0.4

Figure 2. *FESEM images of (a) pure polyaniline (PANI), (b) PCB5 and (c) PCB10 composite samples. EDX spectra of (d) PCB5 and (e) PCB10 composite samples*

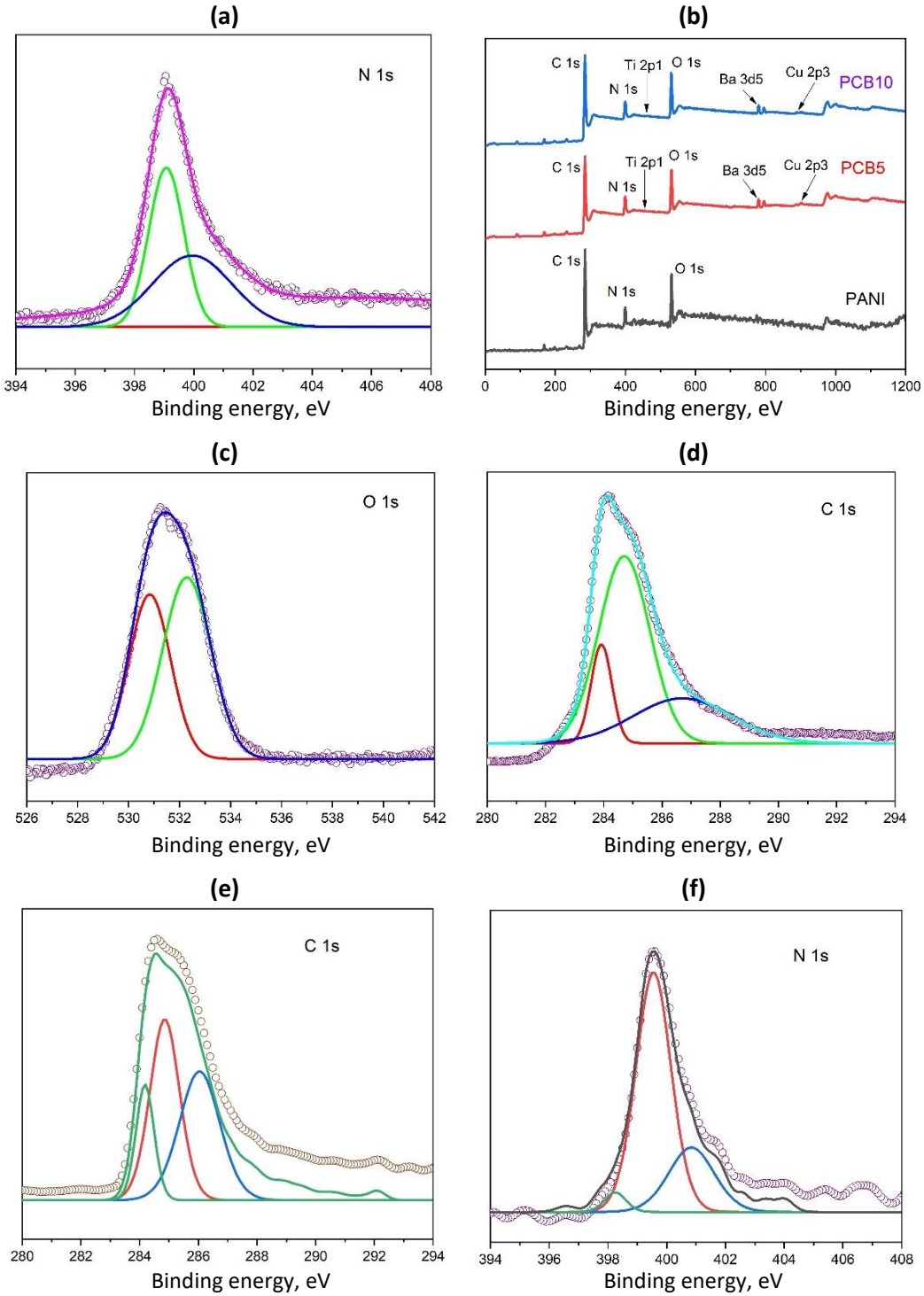

Figure 3. *XPS wide spectra of (a) PANI, BCB5 and PCB10 composite samples, and deconvoluted peaks of (b) O 1s, (c) C 1s, (d) N 1s in PCB5, and deconvoluted peaks of (e) C 1s, (f) N 1s in PANI*

In addition, slight shifts in the peak binding energy positions of Ba 3d, Ti 2p and Cu 2p peaks, as shown in Table 1, suggest electronic interactions between the dopant particles and the polymer matrix, likely arising from chemical bonding or interfacial polarization effects. Figures 3(b) to 3(d) respectively, denote the deconvoluted peaks of O 1s, C 1s and N 1s peaks of PCB5 composite. Deconvolution of the C 1s and N 1s core-level spectra reveals further shifts in peak positions and variations in relative intensities compared to pristine PANI, indicating changes in the local chemical environments of carbon and nitrogen functionalities. Figure 3(e) indicates deconvoluted peak positions of C 1s at binding energies ~284.2, ~284.9 and ~286.1 eV corresponding to (C-C/C-H), (C-N)

and (C=N) bonds, respectively. In Figure 3(f), the N 1s has contributions from imine group (=N-) at ~398.2 eV, amine group (-NH-) at ~399.5eV, and protonated imine group (-N^+-) at ~400.9 eV. Both the C 1s and N 1s are consistent with the emeraldine salt form of polyaniline [13]. These spectral modifications support the formation of strong interfacial interactions between PANI chains and the incorporated oxides. Importantly, the primary peak positions remain consistent with literature-reported values for $BaTiO_3$ and CuO, thereby validating the phase identity of the dopants and the structural integrity of the composite system.

The parameters listed in Table 1 include the start, peak, and end binding energies, eV; peak intensity, count *per* second (CPS); full width at half maximum (FWHM, eV); peak area *P* / CPS eV and content, at.%.

Table 1. *Surface parameters of PCB10 and BCP5 composite samples obtained from XPS spectra analysis*

	Name	Binding energy, eV			Peak intensity, CPS	FWHM, eV	*P* / CPS eV	Content, at.%
		Start	Peak	End				
PCB10	C1s	295.5	284.68	277	392432.86	4.86	2071483.05	71.59
	O1s	538.5	531.43	524.5	233495.08	4.75	1172437.46	16.22
	N1s	410	399.29	391	99552.84	4.71	538362.73	11.81
	Ba3d5	787	780.27	774	47157.4	4.39	225696.66	0.35
	Ti2p1	466	464.65	462	545.3	0.69	1106.73	0.02
	Cu2p3	942	935.19	929	1383.84	1.5	5903.25	0.02
PCB5	C1s	295	284.43	277	440031.33	4.93	2338790.2	74.12
	O1s	539	531.22	523	242396	4.77	1216310.69	15.43
	N1s	410	399.4	391	94011.2	4.79	502309.18	10.11
	Ba3d5	786	780.28	774.5	45421.18	4.45	212108.16	0.3
	Ti2p1	466	465	462	727.64	0.81	743.6	0.01
	Cu2p3	942	933	929	1834.53	0.16	11437.05	0.03

Figure 4 shows the Raman spectra of pure PANI, PCB5, and PCB10. Compared to PANI, both composite samples exhibit enhanced peak intensities and noticeable red-shifts in characteristic PANI bands - particularly in the C=N stretching (~1580 cm^{-1}) and C-N stretching (~1300 cm^{-1}) modes. These observations indicate strong interfacial interactions between PANI and the oxide fillers. The greater intensity increase for PCB5 *vs.* PANI suggests more significant π-orbital perturbation of PANI by CuO, consistent with the formation of localized charge-transfer complexes seen in PANI/CuO composites [14]. Meanwhile, PCB10 exhibits more pronounced peak shifts to lower wavenumbers (~5 to 10 cm^{-1}), implying increased strain or charge delocalization introduced by higher $BaTiO_3$ loading, in line with strain-induced phonon softening observed in $BaTiO_3$/polymer systems.

The Raman band observed around ≈485 cm^{-1} originates from overlapping vibrational contributions, including the C-H deformation and C=N-C stretching modes of PANI [15], which can extend into this region due to structural disorder, together with the Ba-O stretching vibration characteristic of $BaTiO_3$ nanophases [16]. The pronounced feature observed for PCB10 and PCB5 is primarily associated with the Ba-O stretching mode, confirming the effective incorporation of $BaTiO_3$ and strong interfacial interactions within the PANI matrix [17,18]. Variations in band position and relative intensity among the composites are attributed to differences in nanofiller content and interfacial coupling. CuO exhibits distinct Raman modes at approximately 298, 345 and 630 cm^{-1} [19]. The relative intensity and shift trends correlate with the dielectric and electrical properties of the composites. Thus, stronger PANI-CuO interactions in PCB5 lead to improved conductivity, whereas stressed interfaces, reflecting higher $BaTiO_3$ content, enhance polarization at the expense of carrier mobility in PCB10 samples.

These Raman findings align with existing literature: in $BaTiO_3$/polymer nanocomposites, peak red-shifts are typically observed due to strain and interface effects, and PANI/CuO systems similarly show intensity increases and spectral modifications due to charge-transfer coupling. Thus, Raman analysis here substantiates the compositional control of interfacial chemistry and corroborates the trends observed in the dielectric and electrical characterization.

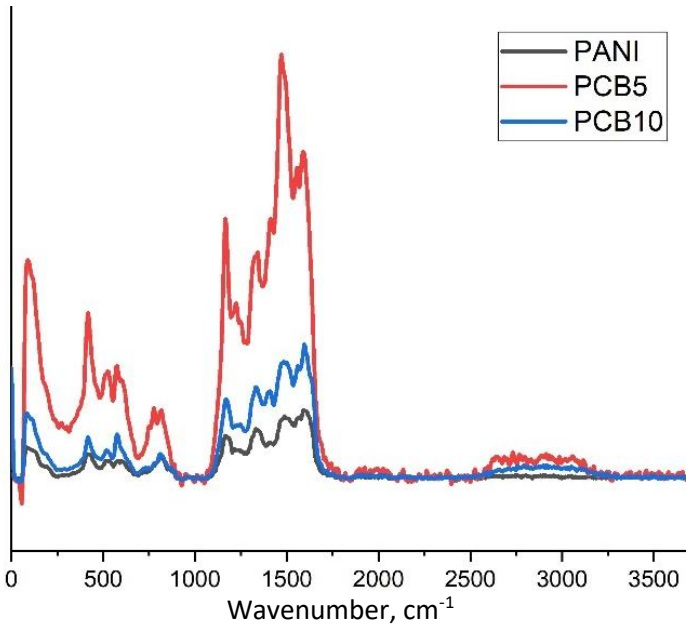

Figure 4. *Raman spectra of PANI, PCB5 and PCB10 composite samples*

Dielectric analysis

Figure 5 illustrates the frequency-dependent dielectric constant (ε'), dielectric loss (ε''), impedance (Z) and AC conductivity (σ_{ac}) of pure PANI and its composites PCB5 (PANI/CuO 10 wt.% / / $BaTiO_3$ 5 wt.%) and PCB10 (PANI/CuO 5 wt.% / $BaTiO_3$ 10 wt.%). All samples exhibit a marked drop in ε', ε'' and Z' at low frequencies, followed by a gradual plateau at higher frequencies. This behaviour is characteristic of Maxwell-Wagner-Sillars interfacial polarization, where charge carriers accumulate at phase boundaries under low-frequency fields, enhancing polarization and losses, which diminish as the field frequency exceeds the interfacial relaxation frequency [20].

- Dielectric constant and loss: PCB10 presents higher ε' and ε'' than PCB5 throughout the frequency range, implying that a higher $BaTiO_3$ content (10 wt.%) reinforces interfacial dipoles and polarization density. Dielectric constant and dielectric loss of hybrid composites (HC) are reduced by increasing the weight percentage of CuO nano buds due to p-type semiconductor behaviour, unmodified surface and size of conducting CuO nano rods [21].
- AC conductivity (σ_{ac}): Each sample maintains nearly constant conductivity at low frequencies (the “DC-like” plateau) before exhibiting a dispersive increase at higher frequencies, consistent with a Jonscher power-law $\sigma_{ac} = \sigma_{dc} + A\omega^n$ [22]. PCB5 outperforms PCB10 in σ_{ac}, indicating that the higher CuO loading (10 wt.%) establishes more efficient percolative hopping paths for charge transport, whereas increased $BaTiO_3$ content in PCB10 may disrupt these pathways.
- Impedance (Z): PCB10 registers a lower real impedance compared to PCB5 across the full frequency spectrum, consistent with enhanced dielectric screening and interfacial polarization in the presence of higher $BaTiO_3$ content [23].

These observations underscore the critical interplay between filler composition and electrical responses: while increased $BaTiO_3$ content boosts dielectric permittivity and reduces impedance,

optimal CuO loading facilitates conductivity. This finely balanced composition tuning aligns with trends reported in the literature for PANI/oxide composites [24].

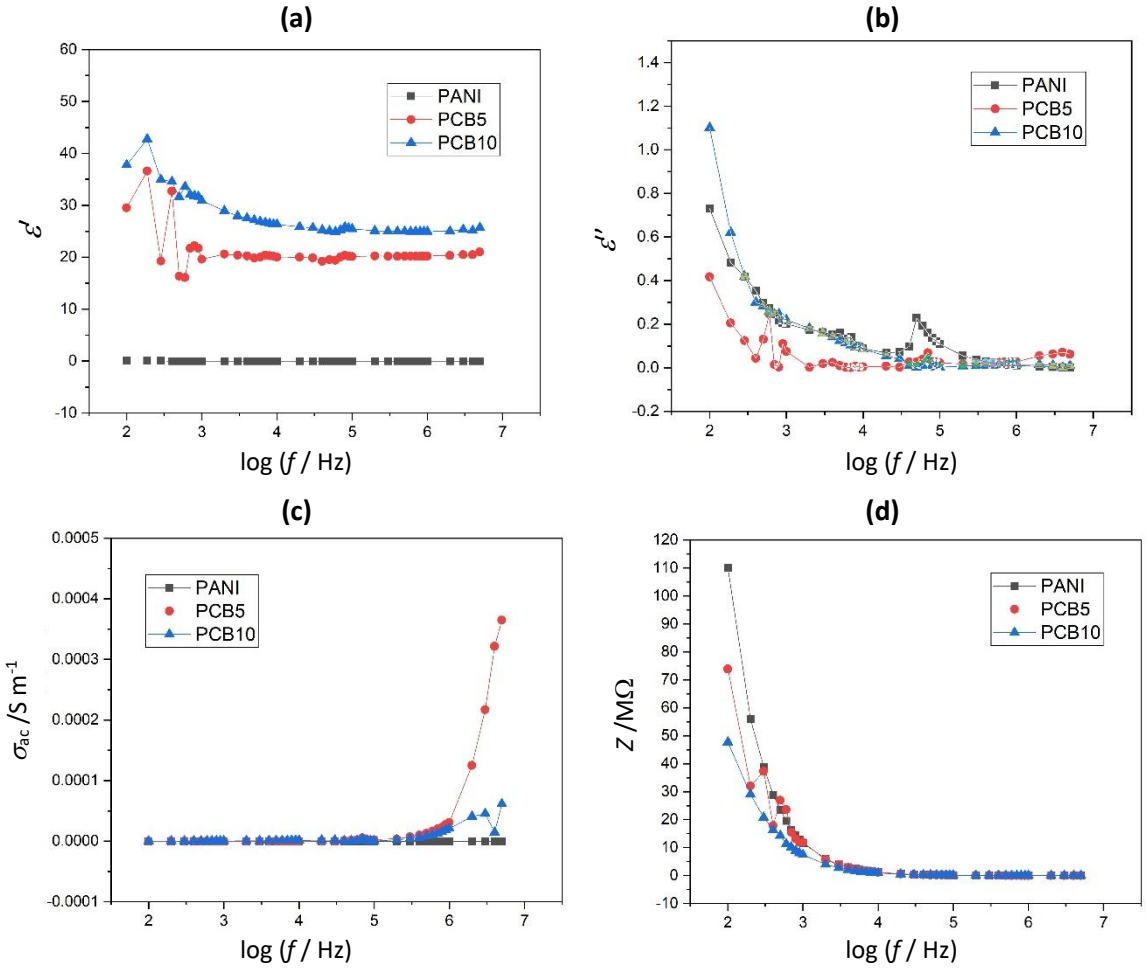

Figure 5. *Frequency-dependent variation of (a) dielectric constant, (b) dielectric loss, (c) AC conductivity, and (d) impedance for PANI, PCB5 and PCB10 composite samples*

Electrochemical analysis

Cyclic voltammetry analysis

In Figure 6(a), the cyclic voltammograms of PANI, PCB5 and PCB10 composite electrodes in 1 M H_2SO_4 are shown. Pristine polyaniline exhibits two main redox peaks. The typical redox processes in polyaniline emeraldine salt cyclic voltammetry graphs involve oxidation of leucoemeraldine to emeraldine and further oxidation to pernigraniline, with corresponding reduction pathways [25]. The doped composites exhibit more intense redox peaks, slight peak shifts, and new peaks. Pure PANI has a conjugated structure, characterized by many π electrons, which results in its high conductivity and the absence of redox peaks. Doping PANI with metal oxides, on the other hand, causes the conjugated structure to be disrupted, which results in the creation of energy levels inside the bandgap. This makes it possible for redox processes to take place and redox peaks in the CV to become more prominent [26].

The specific capacitance values are obtained from CV using Equation (3) [27]:

$$C_s = \frac{\int ivdv}{2mk\,\Delta V} \tag{3}$$

where C_s denotes specific capacitance, $\int ivdv$ the area of the CV polygon, m the active mass, k the scan rate and ΔV the potential window. The obtained C_s values are tabulated in Table 2.

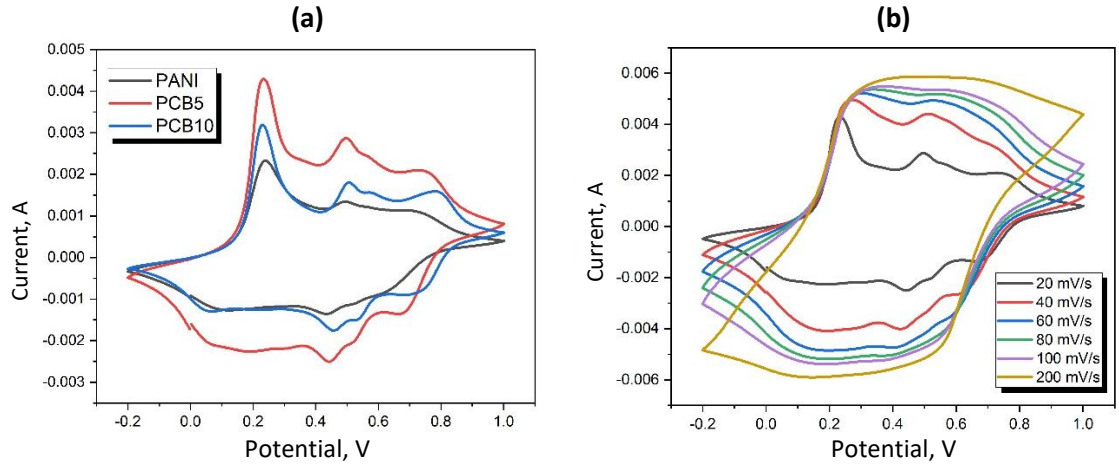

Figure 6. *Cyclic voltammograms of (a) pristine PANI, PCB5 and PCB10 composite electrodes in 1M H_2SO_4 at a scan rate 20 mV s^{-1}, (b) PCB5 electrode at varying scan rates*

Table 2. *Specific capacitance values of PANI, PCB5 and PCB10 electrodes obtained from CV analysis*

Sample	Scan rate, mV s^{-1}	Specific capacitance, F g^{-1}
PANI	20	125.4306
PCB10	20	151.9236
PCB5	20	230.3125
PCB5	40	183.9653
PCB5	60	144.9699
PCB5	80	117.0816
PCB5	100	97.5986
PCB5	200	51.3208

From Figure 6(b) and Table 2, the specific capacitance decreases with increasing scan rate due to the limited time available for charge transfer and ion diffusion within the electrode material. As the scan rate increases, the diffusion of ions to the electrode surface becomes a limiting factor, reducing the effective charge storage capacity [28]. This phenomenon is confirmed by the cyclic voltammetry results, which show that the voltammograms exhibit a quasi-rectangular shape, indicating predominantly capacitive behaviour, while the diffusion process significantly influences the charge storage mechanism.

Galvanostatic charge-discharge analysis

Figure 7(a) shows the GCD curves of PANI, PCB5 and PCB10 electrodes. PCB5 shows a higher specific capacitance than PCB10. From the dielectric studies, it can be seen that $BaTiO_3$ contributed more to the dielectric constant, while CuO contributed to the material's higher conductivity. In electrochemical studies, the enhanced performance is primarily attributed to the high electrical conductivity imparted by CuO, whereas in solid-state dielectric measurements, the improvement is mainly governed by the high dielectric constant of $BaTiO_3$. Shah *et al.* emphasized that the high electrical conductivity of electrode materials significantly enhances the specific capacitance of supercapacitors by facilitating efficient charge transfer [29]. This correlation is critical for optimizing energy storage performance, as it directly influences both energy and power density. Moreover, they report that high ionic and electronic conductivity in both the electrolyte and electrode materials enables rapid ion transport, which is essential for achieving superior specific capacitance in supercapacitor systems.

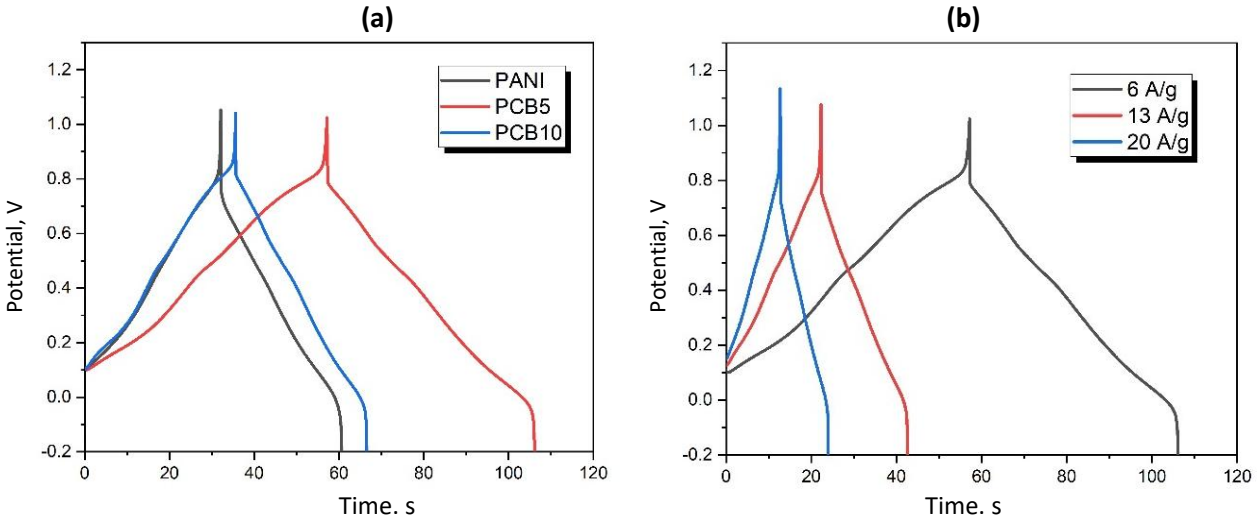

Figure 7. *GCD graphs of (a) pristine PANI, and PCB5 and PCB10 electrodes in 1M H_2SO_4 at current density of 6 A/g, (b) PCB5 at varying current densities*

The specific capacitance values of the samples are calculated from the GCD curves using Equation (4):

$$C_s = \frac{It}{m\,\Delta V} \tag{4}$$

Where, I / A is the discharge current, m / g is the mass of the active material, t is the discharge time, and ΔV is the potential window.

The GCD curves of the PCB5 electrode for different current densities are shown in Figure 7(b)**.** The values of the obtained parameters are noted in Table 3. The maximum specific capacitance was observed at lower current densities, as slower charge-discharge rates allow sufficient time for electrolyte ions to diffuse through the electrode matrix and fully participate in redox reactions. This extended interaction time facilitates more efficient charge storage and utilization of the active material, thereby enhancing the overall capacitive performance of the supercapacitor [30].

Table 3. *Specific capacitance values of PCB5 and PCB10 electrodes obtained from GCD analysis*

Sample	Current density, A g^{-1}	Specific capacitance, F g^{-1}
PANI	6	158.33
PCB10	6	171.67
PCB5	6	271.67
PCB5	13	225.56
PCB5	20	188.32

Electrochemical impedance spectroscopy

The Nyquist plots shown in Figure 8(a) illustrate the impedance behaviour of three samples: pristine polyaniline (PANI), PANI doped with 10 wt.% CuO and 5 wt.% $BaTiO_3$ (PCB5), and PANI with 5 wt.% CuO and 10 wt.% $BaTiO_3$ (PCB10). Each plot comprises a characteristic semicircular region at high frequencies, followed by a near-linear tail at low frequencies. The high-frequency semicircle corresponds to the charge-transfer resistance (R_{ct}) coupled with double-layer capacitance (C_{dl}) at the electrode-electrolyte interface, while the low-frequency linear portion arises from ion diffusion within the porous electrode, indicating diffusion-controlled pseudocapacitive behaviour. The diameter of the semicircle, directly proportional to R_{ct}, reflects the ease of charge transfer, where a smaller semicircle implies improved interfacial charge kinetics and lower R_{ct} [31].

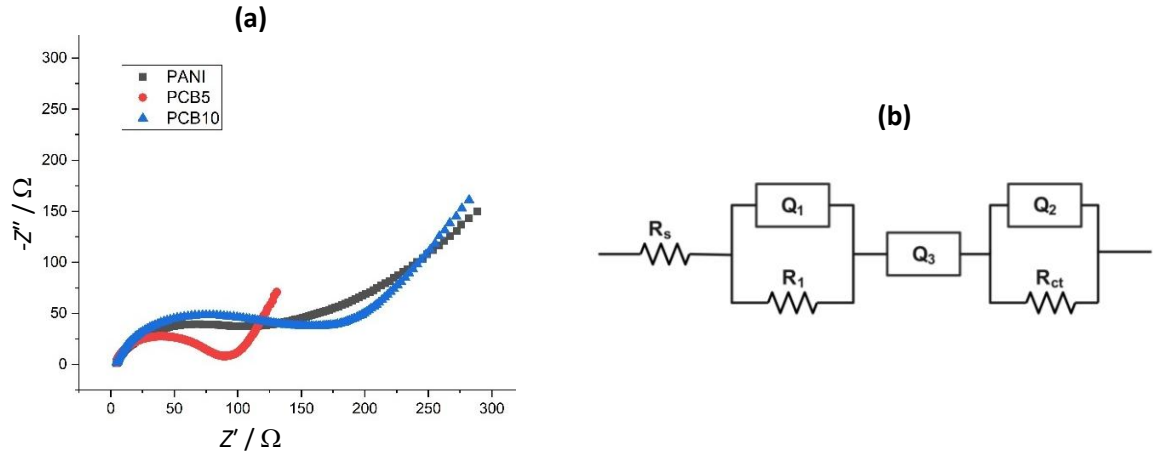

Figure 8. *EIS spectra of (a) pristine PANI and PCB5 and PCB10 composite electrodes in 1 M H_2SO_4 at open-circuit potential (~0 V vs. Ag/AgCl), (b) electrical equivalent circuit used for fitting*

To accurately capture this response, the impedance data were fitted using the equivalent circuit shown in Figure 8(b), where capacitive and/or diffusion responses are described by constant-phase elements (CPE) characterized by impedance parameters *Q* and *n* [31]. Here, Q is the CPE constant (in $S \cdot s^n$), representing the magnitude of the pseudo-capacitance, and n ($0 \leq n \leq 1$) is the exponential factor that indicates the deviation from ideal capacitive behaviour ($n = 1$ corresponds to a pure capacitor and n = 0 to a pure resistor). Differentiation between capacitive and diffusion responses can be made after comparing the values of the exponential factor *n*, which would be close to 1 for capacitive and 0.5 for diffusion responses. The fitted parameters in Table 4 confirm that the PCB5 composite electrode exhibits the lowest R_1 (15.0 Ω) and R_{ct}(5.4 Ω), consistent with the smallest semicircle in the Nyquist plot, indicating superior charge-transfer kinetics and reduced interfacial resistance compared to PCB10 and pristine PANI. This enhancement is attributed to the higher CuO content in PCB5, which improves electron conductivity, thereby facilitating more efficient redox activity at the interface. The series resistance (R_s), which accounts for the intrinsic resistances of the electrode, electrolyte, and contact interfaces, follows a similar trend, lowest for PCB5 and highest for pristine PANI, further supporting the beneficial role of CuO in enhancing charge transport.

Table 4. *Impedance parameter values for PANI, PCB10 and PCB5 electrodes obtained from EIS analysis*

Sample	R_s / Ω	Q_1 / μS s^{n_1}	n_1	R_1 / Ω	Q_2 / mS s^{n_2}	n_2	R_{ct} / Ω	Q_3 / mS s^{n_3}	n_3
PANI	4.104	10.75	0.90	50.53	0.13	0.97	44.45	0.0048	0.44
PCB10	4.017	84.36	0.50	35.10	0.036	0.83	30.39	0.0058	0.49
PCB5	3.945	26.60	0.77	15.02	30.9	1.00	5.387	0.019	0.89

Surface area analysis

The BET analysis is a technique that relies on the physical adsorption of gas molecules, such as nitrogen, onto a solid surface. This method is employed to determine the specific surface area and pore size distribution of materials by measuring the volume of gas adsorbed at low temperature [32]. It accounts for the total surface area of a material, encompassing both external surfaces and internal surfaces within pores. The surface area values obtained in the BET analysis are shown in Table 5. The BET surface area analysis revealed that PCB5 exhibits the highest specific surface area among the samples. This enhancement is attributed to an optimum dispersion of 10 wt.% CuO and 5 wt.% $BaTiO_3$ nanoparticles within the PANI matrix. The smaller CuO particles (~80 nm) act as templating centres, preventing PANI chain restacking and promoting the formation of a more open, porous morphology. The limited amount of $BaTiO_3$ (~5 wt.%) contributes to structural stability and

interfacial roughness without significantly blocking the pores. In contrast, the higher $BaTiO_3$ loading in PCB10 (10 wt.%) leads to particle agglomeration[33] and partial pore blockage due to its larger size (~100 nm), resulting in a lower accessible surface area. Pristine PANI, lacking these oxide interfaces, exhibits the smallest surface area due to compact chain packing.

Table 5. *Surface area of PANI, PCB5 and BCB10 composite samples obtained from BET analysis*

Sample	Specific surface area, $m^2 g^{-1}$
PANI	24.08
PCB5	31.37
PCB10	26.42

Conclusion

The development of multifunctional electrode materials that synergize dielectric enhancement with superior electrochemical performance remains a key challenge in advancing next-generation energy storage systems. In this study, CuO and $BaTiO_3$ nanoparticles were successfully synthesized and strategically incorporated into a polyaniline matrix to engineer two distinct nanocomposites. Comprehensive structural and morphological analyses confirmed the successful integration and uniform dispersion of the dopants. Dielectric characterization revealed that PCB10, with higher $BaTiO_3$ content, exhibited the maximum dielectric constant, while PCB5, enriched with CuO, demonstrated the highest AC conductivity. Electrochemical studies underscored the superior performance of PCB5, which achieved a specific capacitance of 271.67 F g^{-1}, at a current density of 6 A g^{-1}. The enhanced performance was further supported by EIS data, which showed the lowest R_s and R_{ct} values for PCB5, and also, an increased BET surface area of 31.37 $m^2 g^{-1}$ compared to 24.08 $m^2 g^{-1}$ for pristine PANI.

These results highlight the critical role of composition tuning between conductive and dielectric nanofillers in optimizing charge transport, interfacial polarization and energy storage behaviour. The material design strategy presented here offers a promising framework for future exploration of hybrid nanocomposites with tailored functionalities, potentially paving the way for the development of scalable, high-performance electrode materials for supercapacitor and hybrid energy storage applications.

Acknowledgement: *The authors acknowledge the support of the Department of Science and Technology, New Delhi, through the FIST (SR/FST/College-2024/1566 dated 20 December 2024) program for funding this research project. One of the authors is also thankful for the support of Science Engineering Research Board (SERB), New Delhi, Govt. of India (YSS / 2014 / 000649 dated 20 November 2015), for funding the project. We acknowledge Mahatma Gandhi University, Kerala, India for the University Junior Research Fellowship (4446/AC A 6/2022/M.G. U dated 28/04/2022). The authors thank Indian Science Technology and Engineering Facilities Map (I-STEM), a Program supported by the Office of the Principal Scientific Adviser to the Govt. of India, for enabling access to the confocal Raman microscope in conjunction with an AFM [WITec ALPHA 300RA Germany] at MGU Kottayam to carry out this work.*

Declaration of generative AI and AI-assisted technologies in the writing process: *During the preparation of this work the authors used Grammarly to improve the readability and language of the manuscript. After using this tool, the authors reviewed and edited the content as needed and take full responsibility for the content of the published article.*

Compliance with ethical standards: *All authors certify that they have no links with or involvement in any organization or entity that has a financial or non-financial interest in the subject matter, or materials covered in this manuscript.*

***Declaration of competing Interest**: The authors state that they have no known competing financial interests or personal ties that could have seemed to affect the work reported in this study.*

***Research data policy and data availability statement:** The data of this work will be available on reasonable request*

***Credit authorship contribution statement:** Geethu Joseph: methodology, investigation, formal analysis, writing - original draft; Aryadevi Gopinath: investigation, data curation, resources; Veena Rose Mathew: data curation, formal analysis; Alex Jose: formal analysis, investigation; Alex Joseph: validation, data curation; Santhosh Kumar Raghavan Pillai: investigation, resources; Esha Devaraj Suja: Validation; Ginson P. Joseph: supervision, writing, review & editing.; The final version of the manuscript has been approved by all authors.*

References

[1] P. Simon, Y. Gogotsi, Materials for electrochemical capacitors, *Nature Materials* **7** (2008) 845-854. https://doi.org/10.1038/nmat2297

[2] B. E. Conway, *Capacitance Behavior of Films of Conducting, Electrochemically Reactive Polymers*, in: *Electrochemical Supercapacitors*, Springer, Boston, MA, USA, 1999, p. 299-334. https://doi.org/10.1007/978-1-4757-3058-6_12

[3] G. A. Snook, P. Kao, A.S . Best, Conducting-polymer-based supercapacitor devices and electrodes, *Journal of Power Sources* **196** (2011) 1-12. https://doi.org/10.1016/j.jpowsour.2010.06.084

[4] S. Reddy, B. E. Kumara Swamy, H. Jayadevappa, CuO nanoparticle sensor for the electrochemical determination of dopamine, *Electrochimica Acta* **61** (2012) 78-86. https://doi.org/10.1016/j.electacta.2011.11.091

[5] X. Zhu, J. Wang, Z. Zhang, J. Zhu, S. Zhou, Z. Liu, N. Ming, Atomic-Scale Characterization of Barium Titanate Powders Formed by the Hydrothermal Process, *Journal of the American Ceramic Society* **91** (2008) 1002-1008. https://doi.org/10.1111/j.1551-2916.2007.02227.x

[6] K. Ahmed, F. Kanwal, S. M. Ramay, S. Atiq, R. Rehman, S. Ali, N. S. Alzayed, Synthesis and characterization of $BaTiO_3$/polypyrrole composites with exceptional dielectric behaviour, *Polymers* **10** (2018) 1273. https://doi.org/10.3390/polym10111273

[7] N. T. Nagaraj, J. Sannappa, M. Pari, V. N. Krishnanaik, R. Shet, M. Rajashekar, Polyaniline Ingrained Copper Oxide (PANI/CuO) Nanocomposites for Effective Electromagnetic Interference Shielding and Their Sensitive Detection of Dopamine, *Analytical and Bioanalytical Electrochemistry* **16** (2024) 628-642. https://www.doi.org/10.22034/abec.2024.714686

[8] N. A. Abdallah, S. A. Ahmed, M. Almaghrabi, Y. M. Alahmadi, Utilization of a TiO_2-CuO Bimetallic/Polyaniline Nanocomposite as a Transducer in a Solid Contact Potentiometric Sensor for the Determination of Vildagliptin, *Polymers* **15** (2023) 3991. https://doi.org/10.3390/polym15193991

[9] L. Feng, R. Wang, Y. Zhang, S. Ji, Y. Chuan, W. Zhang, B. Liu, C. Yuan, C. Du, In situ XRD observation of CuO anode phase conversion in lithium-ion batteries, *Journal of Material Science* **54** (2019) 1520-1528. https://doi.org/10.1007/s10853-018-2885-0

[10] M. Wu, J. Long, G. Wang, A. Huang, Y. Luo, S. Feng, R. Xu, Hydrothermal Synthesis of Tetragonal Barium Titanate from Barium Hydroxide and Titanium Dioxide Under Moderate Conditions, *Journal of the American Ceramic Society* **82** (1999) 3254-3256. https://doi.org/10.1111/j.1151-2916.1999.tb02235.x

[11] M. Kahouli, A. Barhoumi, A. Bouzid, A. Al-Hajry, S. Guermazi, Structural and optical properties of ZnO nanoparticles prepared by direct precipitation method, *Superlattices and Microstructures* **85** (2015) 7-23. https://doi.org/10.1016/j.spmi.2015.05.007

[12] J. Xue, Q. Yang, R. Guan, Q. Shen, X. Liu, H. Jia, Q. Li, High-performance ordered porous Polypyrrole/ZnO films with improved specific capacitance for supercapacitors, *Materials Chemistry and Physics* **256** (2020) 123591. https://doi.org/10.1016/j.matchemphys.2020.123591

[13] S. Rajkumar, J. Christy Ezhilarasi, P. Saranya, J. Princy Merlin, Fabrication of $CoWO_4$/PANI composite as electrode material for energy storage applications, *Journal of Physics and Chemistry of Solids* **162** (2022) 110500. https://doi.org/10.1016/j.jpcs.2021.110500

[14] S. Abirami, E. Kumar, A review on metal oxide-doped polyaniline nanocomposites, *Journal of Material Science* **59** (2024) 14141-14171. https://doi.org/10.1007/s10853-024-10020-z

[15] C. Yin, L. Gao, F. Zhou, G. Duan, Facile Synthesis of Polyaniline Nanotubes Using Self-Assembly Method Based on the Hydrogen Bonding: Mechanism and Application in Gas Sensing, *Polymers* **9** (2017) 0544. https://doi.org/10.3390/polym9100544
[16] Y. Shiratori, C. Pithan, J. Dornseiffer, R. Waser, Raman scattering studies on nanocrystalline $BaTiO_3$ Part I—isolated particles and aggregates, *Journal of Raman Spectroscopy* **38** (2007) 1288-1299 https://doi.org/10.1002/jrs.1764
[17] K. Anju, K. Roopitha, L.K. Alexander, $BaTiO_3$ SERS substrates for Dimethyl phthalate detection, *Materials Today: Proceedings* **46** (2021) 3044-3050. https://doi.org/10.1016/j.matpr.2021.01.843
[18] S. Chen, X. Lv, X. Han, H. Luo, C. R. Bowen, D. Zhang, Significantly improved energy density of $BaTiO_3$ nanocomposites by accurate interfacial tailoring using a novel rigid-fluoro-polymer, *Polymer Chemistry* **9** (2018) 548-557. https://doi.org/10.1039/C7PY01914A
[19] S. Guha, D. Peebles, J. Terence Wieting, Raman and infrared studies of cupric oxide, *Bulletin of Materials Science* **14** (1991) 539-543. https://doi.org/10.1007/BF02744682
[20] T. Machappa, M. V. N. Ambika Prasad, AC conductivity and dielectric behavior of polyaniline/sodium metavenadate (PANI/$NaVO_3$) composites, *Physica B* **404** (2009) 4168-4172. https://doi.org/10.1016/j.physb.2009.07.194
[21] C. M. B. Krishna, M. Challa, R. Gopal, B. M. Naghabhushana, P. R. Deepthi, International Conference on Advances in Materials, Ceramics and Engineering Sciences (AMCES-2020), Investigation of the dielectric properties of hybrid composite derived from PANI-CuO nano buds, *AIP Conference Proceedings* **2399** (2023) 020017. https://doi.org/10.1063/5.0132547
[22] A. Khan, A. Habib, A. Afzal, High permittivity, breakdown strength, and energy storage density of polythiophene-encapsulated $BaTiO_3$ nanoparticles, *Beilstein Journal of Nanotechnology* **11** (2020) 1190-1197. https://doi.org/10.3762/bjnano.11.103
[23] K. F. Qasim, M. A. Mousa, Effect of Oxidizer on PANI for Producing $BaTiO_3$@PANI Perovskite Composites and Their Electrical and Electrochemical Properties, *Journal of Inorganic and Organometallic Polymers and Materials* **32** (2022) 3093-3105. https://doi.org/10.1007/s10904-022-02335-8
[24] N. Maruthi, M. Faisal, N. Raghavendra, B.P. Prasanna, S.R. Manohara, M. Revanasiddappa, Anticorrosive polyaniline-coated copper oxide (PANI/CuO) nanocomposites with tunable electrical properties for broadband electromagnetic interference shielding, *Colloids and Surfaces A* **621** (2021) 126611. https://doi.org/10.1016/j.colsurfa.2021.126611
[25] S. Bousalem, F. Z. Zeggai, H. Baltach, A. Benyoucef, Physical and electrochemical investigations on hybrid materials synthesized by polyaniline with various amounts of ZnO nanoparticle, *Chemical Physics Letters* **741** (2020) 137095. https://doi.org/10.1016/j.cplett.2020.137095
[26] K. Pandiselvi, S. Thambidurai, Chitosan-ZnO/polyaniline ternary nanocomposite for high-performance supercapacitor, *Ionics* **20** (2014) 551-561. https://doi.org/10.1007/s11581-013-1020-0
[27] L. Zhang, H. Gong, Improvement in flexibility and volumetric performance for supercapacitor application and the effect of Ni-Fe ratio on electrode behaviour, *Journal of Materials Chemistry A* **3** (2015) 7607. https://doi.org/10.1039/c4ta06649a
[28] Y. Belazougui, A. Dib, T. Hadjersi, R. Maizia, A. Thomas, S. Martemianov, Exploring Impact of Various Operating Parameters on the Specific Capacitance at the Glassy Carbon/H_2SO_4 Interface: A Comparative Analysis Using Electrochemical Characterization, *ChemistrySelect* **9** (2024) e202400750. https://doi.org/10.1002/slct.202400750
[29] S. S. Shah, Md.A. Aziz, Properties of Electrode Materials and Electrolytes in Supercapacitor Technology, *Journal of Chemistry and Environment* **3** (2024) 1-45. https://doi.org/10.56946/jce.v3i1.309
[30] M. Z. Iqbal, S. Zakar, M. Tayyab, S. S. Haider, M. Alzaid, A. M. Afzal, S. Aftas, Scrutinizing the charge storage mechanism in SrO based composites for asymmetric supercapacitors by diffusion-controlled process, *Applied Nanoscience* **10** (2020) 3999-4011. https://doi.org/10.1007/s13204-020-01542-4
[31] A. Lasia, *Electrochemical Impedance Spectroscopy and its Applications* in *Modern Aspects of Electrochemistry*, *Vol 32*, B. E. Conway, J. O'M. Bockris, R. E. White Eds., Kluwer Academic / Plenum Publishers, New York, USA, 1999, p. 143-248. https://doi.org/10.1007/0-306-46916-2_2
[32] M. Jaroniec, M. Kruk, A. Sayari, Adsorption methods for characterization of surface and structural properties of mesoporous molecular sieves, *Studies in Surface Science and Catalysis* **117** (1998) 325-332. https://doi.org/10.1016/S0167-2991(98)81008-2

[33] X. Zhang, S. Wei, N. Haldolaarachchige, H. A. Colorado, Z. Luo, D. P. Young, Z. Guo, Magnetoresistive conductive polyaniline-barium titanate nanocomposites with negative permittivity, *The Journal of Physical Chemistry C* **116** (2012) 15731. 15740. https://doi.org/10.1021/jp303226u